Author/s:
Green, H;Gleadow, A;Levchenko, VA;Finch, D;Myers, C;McGovern, J;Heaney, P;Pickering, R

Title:
Dating correlated microlayers in oxalate accretions from rock art shelters: New archives of paleoenvironments and human activity

Date:
2021-08-01

Citation:
Green, H., Gleadow, A., Levchenko, V. A., Finch, D., Myers, C., McGovern, J., Heaney, P. & Pickering, R. (2021). Dating correlated microlayers in oxalate accretions from rock art shelters: New archives of paleoenvironments and human activity. Science Advances, 7 (33), https://doi.org/10.1126/sciadv.abf3632.

Persistent Link:
https://hdl.handle.net/11343/287702

GEOCHEMISTRY

Dating correlated microlayers in oxalate accretions from rock art shelters: New archives of paleoenvironments and human activity

Helen Green[1*†], Andrew Gleadow[1†], Vladimir A. Levchenko[2†], Damien Finch[1†], Cecilia Myers[3†], Jenna McGovern[1†], Pauline Heaney[4†], Robyn Pickering[5†]

Oxalate-rich mineral accretions, often found in rock shelters around the world, offer important opportunities for radiocarbon dating of associated rock art. Here, sample characterization and chemical pretreatment techniques are used to characterize the accretions, prescreen for evidence of open-system behavior, and address potential contamination. The results provide stratigraphically consistent sequences of radiocarbon dates in millimeter-scale laminated accretions, demonstrating their reliability for dating rock art, particularly symbolic markings commonly engraved into these relatively soft deposits. The age sequences are also consistent with correlations between distinctive patterns in the layer sequences visible in shelters up to 90 km apart in the Kimberley region of northwestern Australia, suggesting their synchronized formation is not entirely shelter specific but broadly controlled by variations in regional environmental conditions. Consequently, these accretions also offer potential as paleoenvironmental archives, with radiocarbon dating of layers in nine accretions indicating four, approximately synchronous growth intervals covering the past 43 ka.

INTRODUCTION

Oxalate-rich mineral accretions occur widely on rock surfaces found in many parts of the world including caves [e.g., (*1*)], ancient buildings and monuments [e.g., (*2*)], and many important archeological sites, including rock art shelters in Australia (*3*–*7*), North (*8*) and (*9*) South America, South Africa (*1*), and Spain (*10*). Although the presence of calcium oxalate minerals is the defining feature of these accretions, their mineralogy is complex and variable (*11*). The calcium oxalate mineral whewellite ($CaC_2O_4{\cdot}H_2O$) is frequently the most common mineral present but typically occurs together with calcium sulfates, particularly gypsum ($CaSO_4.2H_2O$), and, to a lesser degree, rare phosphate minerals including newberyite ($Mg(PO_3OH){\bullet}3(H_2O)$ and others (e.g., *3*, *5*, *11*, *12*). The origin of calcium oxalate minerals has been widely debated, but there is now a general consensus that their origin is biological (*6*, *13*, *14*), potentially involving cyanobacteria (*15*), micro-stromatolitic algae, fungi (*6*, *16*), or lichens (*2*, *8*, *10*, *17*, *18*). A direct role of animal excretions is also clear in some environments (*1*), but in others, this association may be indirect, facilitating oxalate precipitation by providing additional nutrients for bacterial growth (*11*, *12*).

Globally, oxalate-rich accretions have been found on rock art panels, with the carbon component of the oxalate mineral providing a clear opportunity for radiocarbon dating of associated motifs (e.g., *4*, *5*, *7*–*9*, *19*, *20*). Radiocarbon dating of oxalate accretions has provided minimum (*5*, *6*, *8*) and, in some cases, bracketing (*21*) ages for associated rock art, although concerns have been raised about the source of the dated carbon, the possibility of open-system behavior in the accretions, and possibilities of sample contamination by either older or younger organic constituents (*22*). Chemical pretreatment procedures (*5*, *23*) have been used with apparent success in dating studies to isolate pure oxalates from other organic materials present, suggesting that some of these risks can be avoided or controlled by improved analytical protocols and a better understanding of the dated materials. However, identifying the source of the dated carbon in such oxalate minerals requires an understanding of their formation mechanism and is essential in relating radiocarbon dates to the time of mineral formation, which may, in turn, be related to associated rock art.

The biological agencies involved in the formation of oxalate-rich mineral accretions (*2*, *13*, *16*, *17*, *24*) imply that the carbon source in the oxalates is derived directly from contemporaneous atmospheric carbon dioxide. There appears to be no carbon exchange with the substrate, even where the oxalates are formed on limestones (*24*), and consequently, radiocarbon dating of oxalate accretions will reliably indicate the timing of formation of a particular layer. Although evidence of weathering has been identified on accretion surfaces in some environments (*11*), oxalate is generally considered to be inert, stable under ultraviolet radiation, and generally insoluble (*20*, *21*). Consequently, in sheltered locations, it has been shown that oxalate-rich accretions can survive for tens of thousands of years (*4*, *5*, *20*, *25*). This longevity, alongside a microbial formation mechanism, suggests that such deposits might preserve records of the conditions under which the accretions formed (*3*, *6*, *17*, *18*), providing dual utility as paleoenvironmental archives on time scales relevant to human occupation and any associated rock art.

Oxalate-rich mineral accretions in the Kimberley region, northwest Australia

The Kimberley region of northwest Australia hosts one of the largest rock art provinces in the world, which, together with numerous

[1]School of Geography, Earth and Atmospheric Sciences, The University of Melbourne, Carlton, Victoria, Australia. [2]Centre for Accelerator Science, Australian Nuclear Science and Technology Organisation (ANSTO), Locked Bag 2001, Kirrawee DC, New South Wales 2232, Australia. [3]Dunkeld Pastoral Co. Pty Ltd Theda Station, PMB 14, Kununurra, Western Australia 6743, Australia. [4]Lettuce Create/Rock Art Australia, 16 Chaucer Parade, Strathpine, Queensland 4500, Australia. [5]Department of Geological Science, Human Evolution Research Institute, University of Cape Town, Rondebosch, 7701 Cape Town, South Africa
*Corresponding author. Email: greenhe@unimelb.edu.au
†These authors contributed equally to this work.

archeological sites, form a record of human activity spanning at least the past 50,000 years (*26*). In the Kimberley, oxalate-rich mineral accretions are particularly well developed and are a near-ubiquitous feature of the thousands of rock shelters found within the Paleoproterozoic orthoquartzites of the Wunaamin Miliwundi (formally King Leopold) and Warton Sandstones of the Kimberley Basin (Fig. 1). Rates of landscape evolution in these competent, durable sandstones are low [~1 m million years^{-1}, meaning that rock surfaces within the shelters may be very long lived (*27*). Consequently, many of the oxalate accretions accumulating in Kimberley rock shelters are relatively thick (up to 5 mm) (*11*) compared to those recorded elsewhere [< 1 mm (*5*, *6*, *8*, *9*)].

Oxalate-rich accretions are one of four distinct mineral accretion systems occurring on Kimberley shelter surfaces, each with a particular field context and mineral association, suggesting slightly different modes of origin (*11*, *12*). The accretions have a dark-brown to black, polished or glaze-like appearance, well-crystallized mineral constituents, and range in thickness up to ~5 mm but are generally <3 mm from the substrate to the surface (*11*, *12*). They are found mostly as extensive smooth coatings on low-angle sandstone surfaces within the drip-line of rock shelters (*11*) (Fig. 1) and occasionally form on small ledges or in crevices on the shelter walls (*3*).

The ubiquity of oxalates throughout the quartz sandstone terrains of northern Australia (*5*, *11*, *12*) demonstrates that carbonates from the substrate are not required in the formation process and that the calcium component must be sourced externally from the local environment. We propose that annual dry season bushfires provide the source of both calcium and other ions (*28*), with the dominant occurrence of the accretions on stable ledges and low-angle shelter surfaces, where they provide a nutrient source for microbial communities that develop during periods of increased moisture availability (*29*). These microbes assimilate carbon from the atmosphere and excrete this in oxalic acid ($C_2H_2O_4$) during metabolization, promoting chelation of cationic constituents (e.g., Ca^{2+}) in the accumulated aeolian material and the formation of a calcium oxalate layer (*13*).

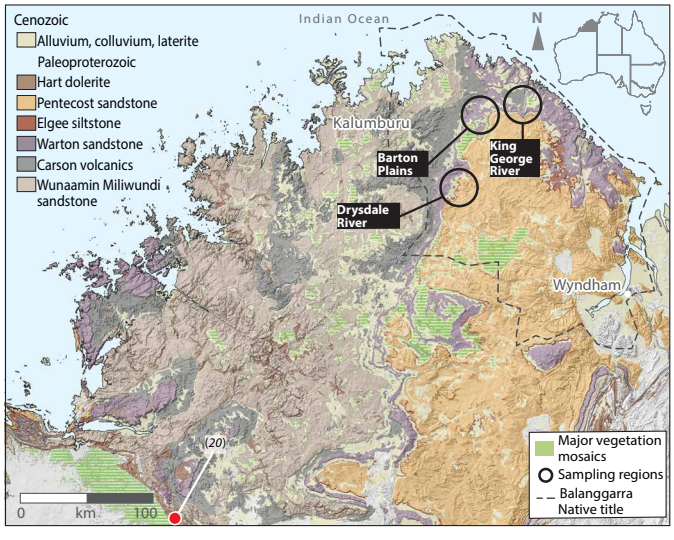

Fig. 1. Map of Kimberley sampling region in Western Australia. Geological map displaying broad sampling regions within the Warton Sandstone Units for nine accretion samples detailed in Fig. 8. The location of similar oxalate-rich, laminated accretions at Carpenter's Gap (*20*) is also highlighted. Illustration adapted from (*12*).

The accretions are also characterized as laminated with distinctive internal stratigraphies of alternating, laterally continuous, light and dark layers of variable thickness (typically ~30 to 150 μm) (*11*, *12*). The preservation of this internal layering suggests that individual layers are progressively shielded from active communication with the growth surface by the deposition of subsequent layers and consequently would be expected to produce sequenced radiocarbon dates, providing an opportunity to test for closed system behavior within the oxalate layers. Lateral continuity of the fine laminations and the larger visible layers also suggests that they have not been disturbed by processes such as dissolution and reprecipitation. If recurring patterns of microlaminations, identified in the cross sections of accretions collected across the northeast Kimberley, can be correlated, then a regional-scale control on formation may be proposed and a master chronology for these distinctive stratigraphies may be produced.

Here, we report on the composition and internal laminated structure of 18 oxalate-rich mineral accretions collected from 16 sandstone rock shelters (Fig. 1), 11 of which relate to rock art. Radiocarbon dates are presented for both the calcium oxalate and inert residue fractions of 28 subsamples from 14 accretions demonstrating both their reliability and their production over a time range comparable to the period of human habitation in the region. The results have important implications for dating the rock art, calibration of geomorphic process rates, and point to the potential of oxalate-rich accretions as archives of paleoenvironmental conditions for this region.

RESULTS

Field observations at Kimberley rock shelters

Oxalate-rich accretions are occasionally associated with painted art (Fig. 2, C and D) but more frequently with patterns of engraved grooves (Fig. 2A) or ground cupules (Fig. 2B), often cut deep into these distinctive surfaces, especially on thicker, more extensive sheets. Engravings usually consist of multiple, roughly parallel, broad V-shaped grooves up to 1 cm wide (Fig. 2A) or less frequently as simple motifs, commonly animal tracks, scratched into the accretion surface. The grinding process used to make the engravings appears to have exploited the much softer nature of the accretion minerals relative to the hard underlying quartzite (*11*, *12*) and internal layering, characteristic of the Kimberley accretions (*11*), is occasionally visible to the naked eye on broken or eroded edges (Fig. 3B).

Internal layering in oxalate-rich accretions

Microscope imaging of the internal structure of the accretions in cross section identified alternating light- and dark-colored layers of varying thickness (typically ~30 to 150 μm) consisting of fine-grained, compact material (Fig. 3C), in many cases, made up of even finer laminations. Most samples contained at least four clearly identifiable layers with distinctive patterns in the occurrence of certain well-defined "marker layers" defined by their color, thickness, and relationship to each other in the sequence. These are particularly evident in the lighter layers and can be seen in accretions collected over an area in excess of 1500 km^2 (Fig. 1). A particular doublet of two relatively thin light-colored marker layers separated by a thin dark layer can be correlated between samples across the region, mostly occurring toward the top of the individual microstratigraphic sequences.

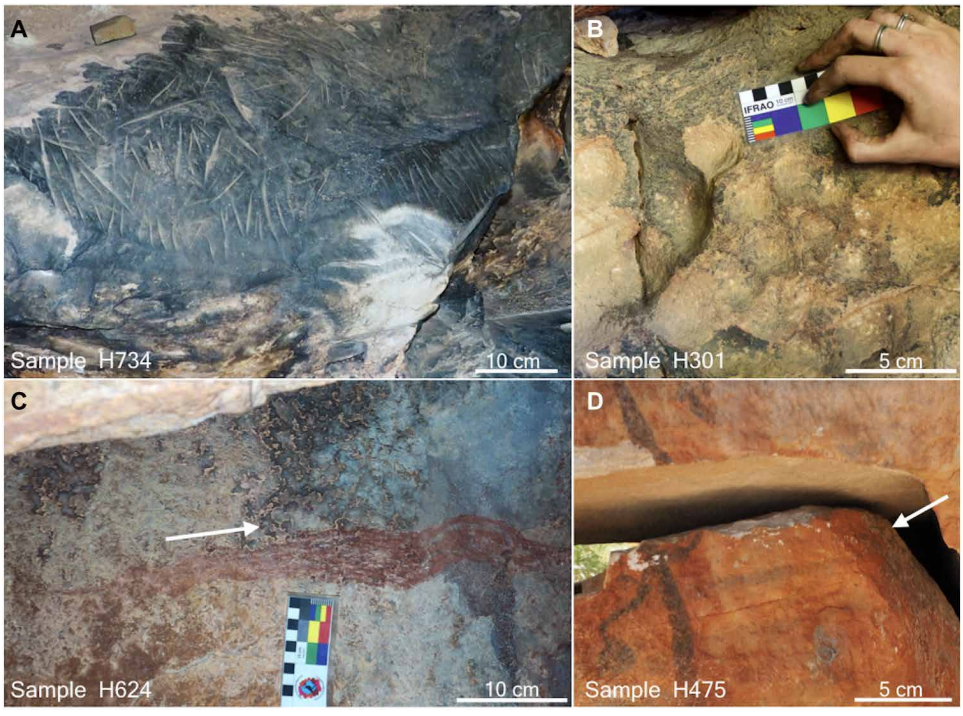

Fig. 2. Examples of the relationship between oxalate-rich mineral accretions and rock art at sites across the Kimberley sampling region. (**A**) Subparallel sets of engraved grooves within a smooth dark oxalate surface (sample H734, Drysdale River). (**B**) Ground cupules penetrating an oxalate-crusted surface (sample H301, Drysdale River). (**C**) Sample H624, Barton Plains, an example of partially corroded glaze-like mineral accretion encroaching down over a painted panel. (**D**) Sample H475, Drysdale River, an example of an oxalate-rich mineral accretion forming in a fracture that has disrupted, and therefore post-dates, the associated painted figure. White arrows identify the oxalate-rich material. See Fig. 1 for sampling regions. Photo credit: (A to D) Cecilia Myers, Dunkeld Pastoral Company.

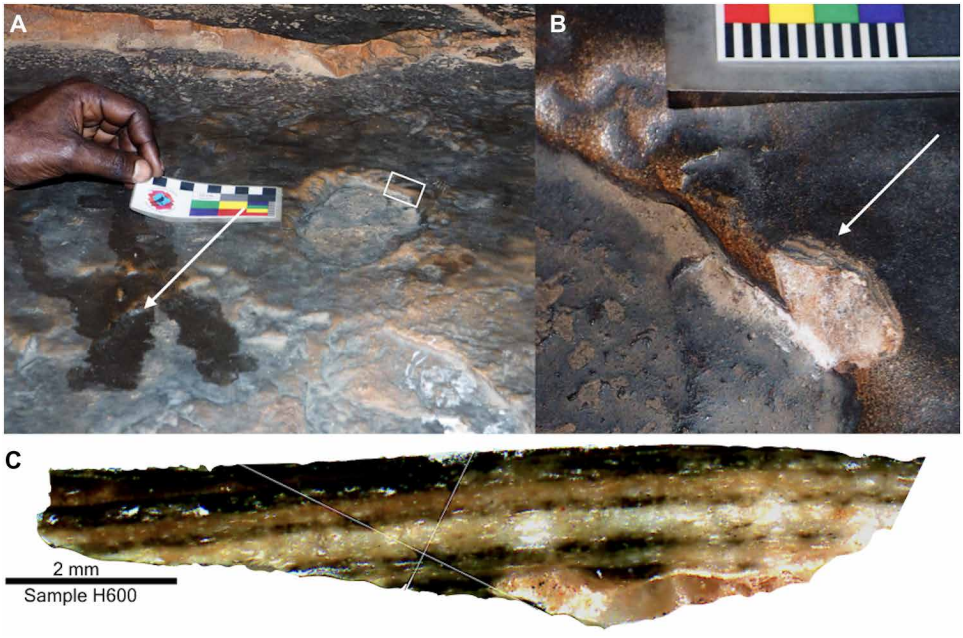

Fig. 3. Accretion sample H600 collected at Barton Plains (Fig. 1). (**A**) Dark-colored, smooth, and dusty mineral accretion coating a low-angle sandstone rock shelter surface. White arrow indicates a patch of fresh animal urine, and white box highlights sample target (H600). (**B**) White arrow indicates internal layering observed in the broken cross section at the accretion sampling site. (**C**) Mounted and polished accretion sample (H600) displaying the internal stratigraphy in cross section. Photo credit: (A and B) Cecilia Myers, Dunkeld Pastoral Company and (C) Helen Green, University of Melbourne.

These patterns in the internal layering of multiple accretions were used to guide sampling of darker oxalate-rich material for radiocarbon dating to investigate whether correlated layers were of the same age and therefore recording a response to a regional scale external agency that influenced accretion formation.

Microcomputed tomography analyses of accretion fragments

Although similar, the alternating layers demonstrate differences in grain size, porosity, and mineral composition, often appearing to be further divided into microlaminae, approximately 10 μm thick, under the microscope. Although microscope imaging enables the continuity of these layers to be assessed in two dimensions, the application of microcomputed tomography (micro-CT) imaging provides a previously unidentified way to assess the internal structure of the accretions in terms of both porosity and the identification of structural inconsistencies (fissures/cavities) in three dimensions. Porosity calculations identify the analyzed accretions to be highly compact in general, although variable through each sample profile (Fig. 4). In many instances, peaks in the porosity profile can be aligned with light-colored layers, suggesting that these layers include a higher proportion of accumulated aeolian material from the surrounding environment imparting a higher porosity (Fig. 4 and movies S1 to S4).

Micro-CT imaging also demonstrates that the horizontal layering within the accretions is laterally continuous in three dimensions, with large pore spaces/voids typically occurring as discontinuous partings between laminations (Fig. 4, black arrows). These pore spaces are masked during image processing and therefore appear black compared to the pale grays of the surrounding laminated material or the darker grays of the underlying quartz sandstone substrate in H076 (Fig. 4C). These horizontal, high-porosity features are also often laterally continuous in three dimensions and demonstrate no communication with the accretion surface; and therefore, no opportunity for the introduction of extraneous carbon once new sealing laminations have been deposited. Similarly, the infrequent small fissures observed (Fig. 4, B and C, red arrows) have limited penetration below the surface, never penetrating the entire accretionary sequence. These features are discontinuous in three dimensions and usually confined to specific regions. Moreover, they appear to be mineralized, which would also prevent further mobilization of surface material into deeper layers. Although these fissures do represent a small risk of younger calcium oxalates penetrating into deeper target layers, micro-CT screening suggests that the possibility of this occurring is almost nonexistent in most cases.

Laser ablation trace element mapping of accretion cross sections

Samples demonstrating clear, consistent layering in cross section and calcium oxalate proportions of >50%, as identified in x-ray diffraction (XRD) analyses (*11*, *12*), were selected for trace element

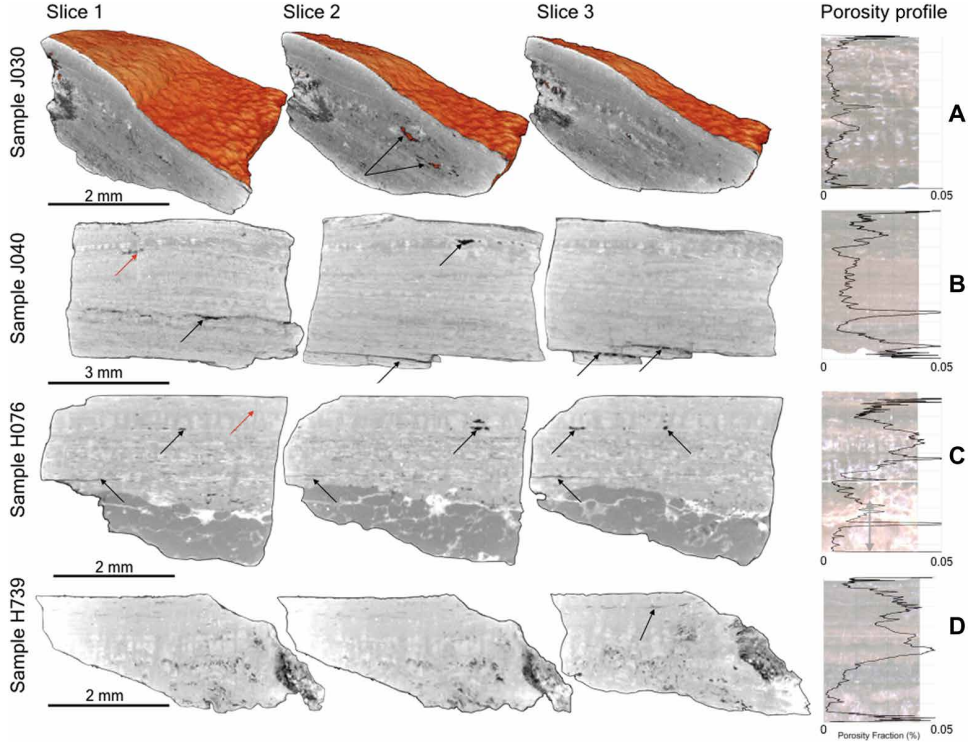

Fig. 4. Micro-CT imaging of four oxalate-rich accretions. Samples J030, H076, J040, and H739 (Table 1; see Fig. 1 for Barton Plains and Drysdale River sampling locations) are displayed as three "slices" perpendicular to the internal layering. (**A**) The orange/brown colors in sample J030 are used to visually represent the hummocky topography of the accretion surfaces, while porosity (e.g., air) is masked out and appears dark gray-black in all samples. (A and **B** to **D**) These features are highlighted with black arrows and occur exclusively as partings between layers and do not connect to the surface. Cracks/fissures within the accretions are comparatively rare and appear to have been infilled with mineral material with a similar density to the surrounding laminations. (B and C) Red arrows indicate examples of these sealed lamination-transgressive cracks/fissures in samples J040 and H076. See movies S1 to S4 for animated progression through the entire accretion fragments. Porosity profiles by layer are also presented for each sample. High porosity measurements at the top and base of each sample are due to uneven surfaces, rather than internal pore space. (C) The gray arrow on sample H076 indicates the quartzite bedrock that makes up the lower ~30% of this sample.

mapping using laser ablation–inductively coupled plasma mass spectrometry (LA-ICPMS). Results for samples H076, H347, H653, and H204 are reported in Fig. 5 and in figs. S1 to S4. On the basis of prior XRD analysis of the bulk mineralogy showing whewellite ($CaC_2O_4{\cdot}H_2O$) and gypsum ($CaSO_4.2H_2O$) to be the most common constituents (*11*, *12)*, the coincident occurrence of relatively high calcium and sulfur concentrations was interpreted to represent gypsum, while relatively high calcium but low sulfur concentrations were assumed to be indicative of whewellite.

Broadly, calcium occurs in higher concentrations in the dark layers of all four analyzed samples (Fig. 5 and figs. S1 to S4). In samples H347 and H204, relatively low sulfur concentrations also occur in the darker layers (figs. S1 and S4), indicating the occurrence of calcium oxalate-rich material, subsequently targeted for radiocarbon dating samples. However, in samples H076 and H653, this relationship is less clear (Fig. 5 and figs. S2 and S3), suggesting the coprecipitation of calcium sulfate and calcium oxalate minerals and that the chemistry of individual layers may reflect relatively rapid fluctuations in formation conditions at the sample site.

All four samples demonstrate high concentrations of aluminum (Al) and silicon (Si) in paler, thinner layers, probably representing clays and quartz in windblown dust accumulating on the formation surfaces of the accretions at certain times. Higher proportions of this windblown dust might represent drier conditions and periods of microbial inactivity (Fig. 5 and figs. S1 to S4).

The relationship between magnesium (Mg) and phosphorus (P) concentrations in the dark and light layers is variable across the four samples (Fig. 5, C and G, and figs. S1 to S4, C and G). Magnesium phosphate minerals such as newberyite ($Mg(PO_3OH){\cdot}3H_2O$) and struvite ($NH_4MgPO_4{\cdot}6H_2O$) and calcium oxalate crystals are commonly found in urine (*10*, *30*), frequently observed in association with oxalate-rich mineral accretions in Kimberley rock shelters (Fig. 3A). The sheltered, shaded, low-angle surfaces likely provide favorable conditions for both microbial activity and local fauna. Many microbes also metabolize phosphorus and contain phospholipids in their structures, and so animal urine may provide an additional nutrient source for microbial activity. The retention of phosphate minerals in the accretion mineralogy would therefore be consistent

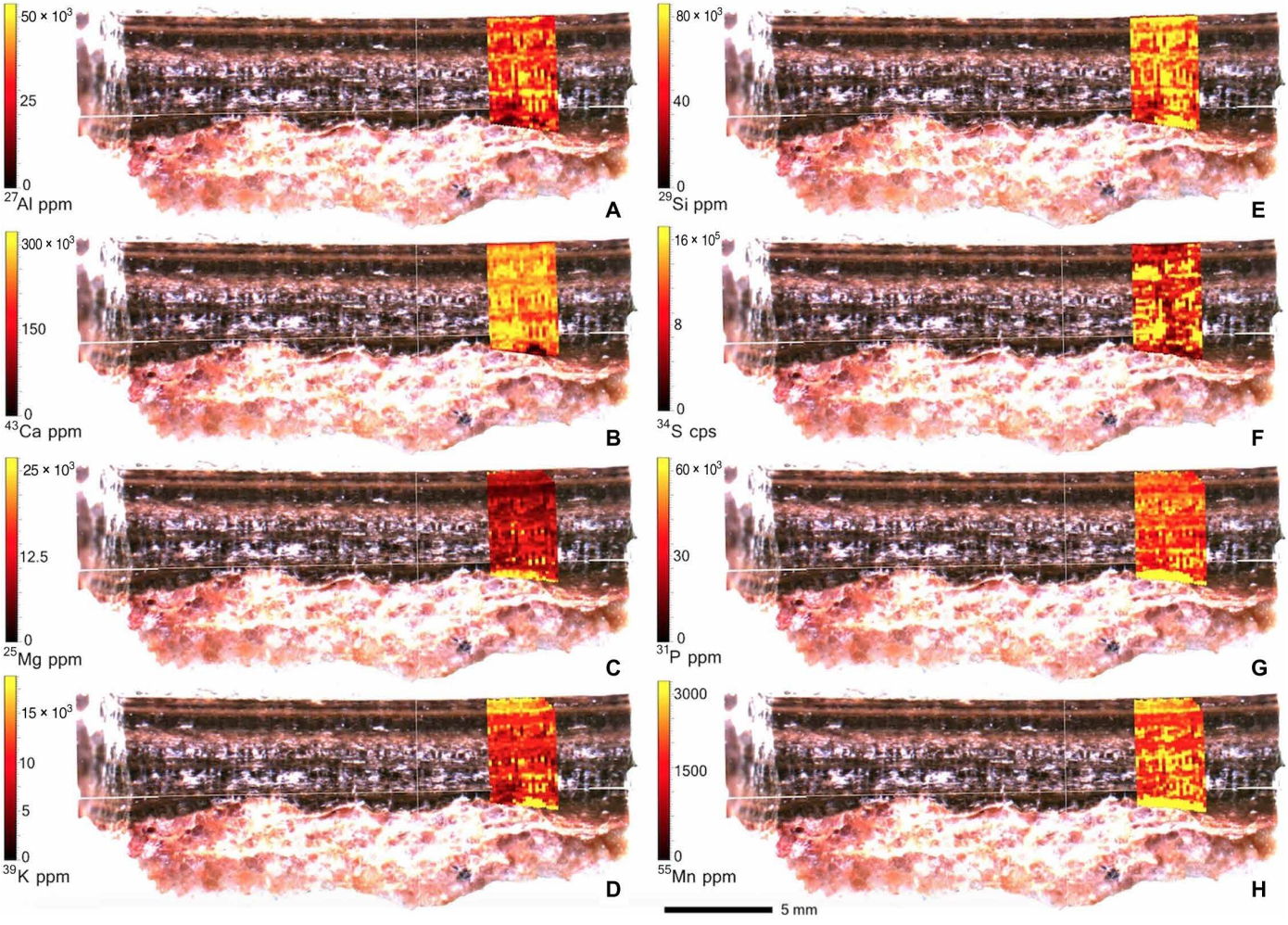

Fig. 5. LA-ICPMS trace element maps for sample H076 in cross section. Elements of interest (Al, Si, Ca, S, Mg, P, K, Mn) to understanding the oxalate-rich accretion formation process and radiocarbon dating potential of the accretions are reported (**A** to **H**). Sulfur content cannot be quantified in LA-ICPMS analyses because standard values are poorly known and sulfur is volatile during the sample preparation and, consequently, values are reported in counts per second (cps). Photo Credit: Helen Green, University of Melbourne. ppm, parts per million.

with a microbiological formation mechanism (*2*, *6*, *10*, *11*, *14*–*18*). Other phosphate minerals and some ammonium signatures were also identified in the XRD analyses of 19 Kimberley accretions, although these constituents are absent in many accretions and therefore apparently not essential to their formation. However, it is notable that XRD analyses will not detect concentrations of <~3% nor will it detect amorphous material and that, consequently, trace levels of phosphates may be present in all samples. Consequently, Mg and P levels in the accretion layers may derive from animal urine, at least in some locations, potentially fixed to these physically stable surfaces through microbiological processes. The more variable distribution of the phosphates suggests that this mechanism may occur during both the intervals of oxalate-rich deposition (darker layers) and intervals of windblown dust accumulation (lighter layers). Higher concentrations of potassium (K) and manganese (Mn) also generally occur in the lighter layers of all four samples (Fig. 5, D and H, and figs. S1 to S4, D and H) and may relate to bushfire ash accumulating during extended intervals less conducive to microbial activity or annually following the dry season.

Electron microprobe mapping of accretion cross sections

Electron microprobe mapping was used to produce two-dimensional maps of key elemental distributions in cross section for sample H748, selected because of its consistent internal layering and oxalate content. Two-dimensional, cross-sectional maps for the elements carbon, sulfur, calcium, and phosphorus (Fig. 6) revealed calcium- and carbon-rich areas, assumed to relate to calcium oxalate (whewellite), and calcium- and sulfur-rich areas, assumed to relate to calcium sulfates (gypsum/anhydrite/bassanite), the dominant minerals in most Kimberley oxalate-rich accretions (*11*, *12*).

However, the microprobe mapping did not identify a clear relationship between the elemental distributions and the alternating dark and light layers in these samples. This suggests that the layers may represent varying proportions of the coprecipitated oxalate and sulfate minerals particularly during transitions between the conditions required for deposition of the two mineral groups. Broadly, sulfur (from the sulfates) occurs in higher concentrations in the darker layers and calcium (in both oxalates and sulfates) occurs in higher concentrations in the lighter layers, while phosphorus occurs in distinct layers but with no clear association to the alternating dark and light layers, as also observed in LA-ICPMS mapping (Fig. 5G and figs. S1 to S4G). A broad relationship between the concentration of carbon and darker colored layers is apparent, suggesting that calcium oxalate is concentrated there (Fig. 6) and used to inform subsampling for radiocarbon dating.

Radiocarbon age measurements from target accretion layers

Radiocarbon dating results from 28 oxalate-rich subsamples that were micromilled from individual layers in 14 separate accretions (Table 1) indicate deposition of these materials occurred between 43.1 and 0.2 ka cal B.P. (using the median value of individual calibrated age estimates). Sequences of up to four radiocarbon ages (per accretion) were produced for acid-soluble fractions across multiple layers in samples J030, H653, H076, and J040. All ages acquired on the acid-soluble fractions, without exception, were found to be in the correct stratigraphic sequence from oldest near the sandstone substrate surface to youngest at the top and demonstrate that, without targeting specific layers, only averaged radiocarbon ages for the entire accretion sequence can be achieved (e.g., Sample H475_bulk versus H475_milled; Table 1). Two subsamples (H076 Middle 1 and H076 Middle 2; Table 1 and Fig. 5) milled from a single layer in sample H076 also returned consistent ages (Table 1). Once a target layer was identified, a larger accretion fragment was set in cross section and sample tracks of ~8 mm in length were milled using a 0.25-mm-width dental drill bit to a depth of 0.25 mm. Once milled, the accretion was repolished to a flat surface, resulting in ~0.5-mm separation in the *z* plane between tracks. A second aliquot was subsequently milled from the same layer.

Stable carbon isotopes were also measured in the acid-soluble fractions where sufficient carbon was available for measurement. These results show $\delta^{13}C$ values of ~−8 to 15 ‰ that conform to a microbiological pathway for their origin. Nonoxalate residues were analyzed for 22 of the subsamples showing different $\delta^{13}C$ values of ~ −25‰ that are more indicative of black pyrogenic carbon particles (Table 1).

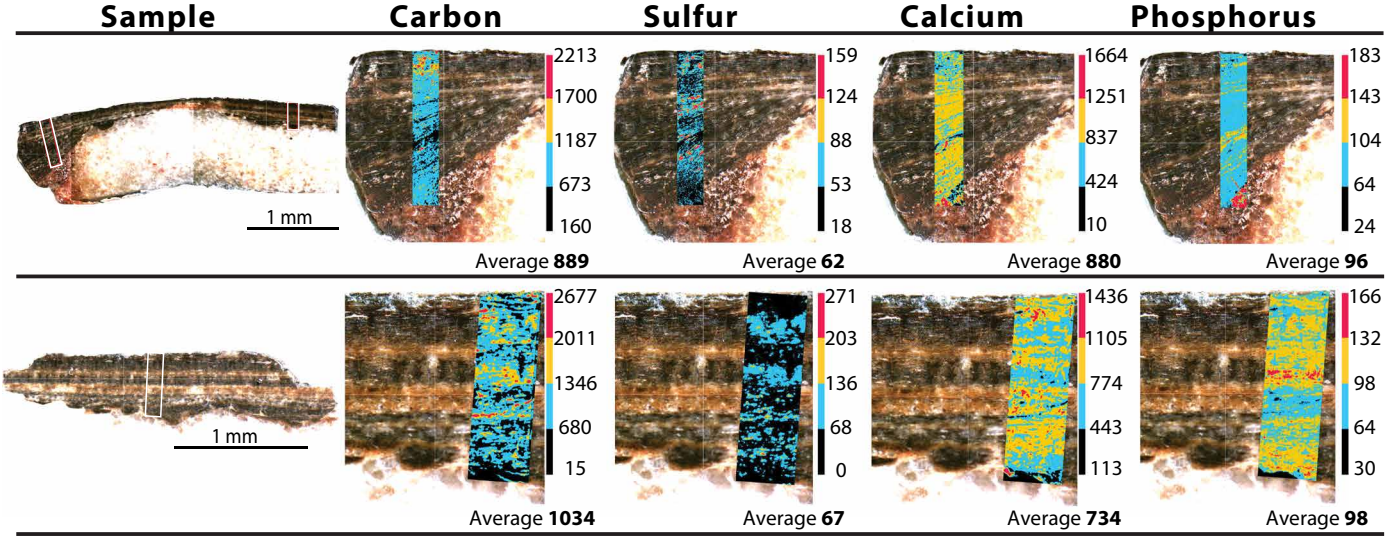

Fig. 6. Electron microprobe mapping of elements such as calcium (Ca), sulfur (S), carbon (C), and phosphorus (P) (counts per second) in two fragments of accretion H748. Photo credit: Helen Green, University of Melbourne.

Table 1. Radiocarbon age measurements on laminated, oxalate-rich mineral accretions from Kimberley rock shelters. Radiocarbon age measurements were determined on both the calcium oxalate and inert residue fractions where sufficient material was available. For a complete description of the pretreatment process, refer to Jones *et al.* (*5*). The $\delta^{13}C$ of −22.5‰ (residue) and −12.1‰ (calcium oxalate) was measured using Elemental Analyser-Isotope MS. All other samples contained too little carbon for this ratio to be measured directly. The typical charcoal (black carbon pyrogenic particles) value for $\delta^{13}C$ (−25 ‰) was assumed for all other residue fractions, and the typical $\delta^{13}C$ oxalate value (−11 ‰) was assumed for all other acid-soluble fractions. Calibrated using CALIB 7.1.0 (*44*) using the Southern Hemisphere dataset (*45*).

Sample code	Laboratory code	$\delta^{13}C$ per mil	C mass (μg)	Mass Err (μg)	Percent modern carbon (pMC)	±1σ error	Calibrated date (95.4% probability range)(years cal. yr B.P.)					
							from	to	%	Median	Discrepancy	Younger/ Older
J030_Top	OZY894U1	−11	10.9	0.1	19.20	1.71	17,720	13,730	95.4	15,780		
J030_Top-Residue	OZY894U2	−25*	33.0	0.3	15.80	0.31	18,367	17,590	95.4	17,985	2205	Older
J030_Middle 1	OZY893U1	−11	57.7	0.6	14.95	0.35	18,850	18,020	95.4	18,470		
J030_Middle 1-Residue	OZY893U2	−25*	131.0	1.3	13.52	0.11	19,565	19,121	95.4	19,347	887	Older
J030_Middle 2	OZY891U1	−11	50.4	0.5	11.25	0.34	21,820	20,550	95.4	21,160		
J030_Middle 2-Residue	OZY891U2	−25*	110.0	1.1	15.51	0.14	18,355	17,929	95.4	18,145	3015	Younger
J030_Base	OZY892U1	−11	43.0	0.4	3.48	0.34	32,780	29,310	95.4	30,960		
J030_Base-Residue	OZY892U2	−25*	63.0	0.6	12.07	0.23	20,823	20,040	95.4	20,430	10,530	Younger
H475_Bulk	OZW429U1	−11.2	410.0	10	78.43	0.24	1750	1770	5.4	1860		
							1810	1920	94.6			
H475_Bulk-Residue	OZW429U2	−25*	122.2	2.2	84.89	0.45	1280	1080	95.4	1210	650	Younger
H475_ Milled	OZW428U1	−11.0	14.1	0.14	95.96	1.43	0	30	3.1	335		
							60	120	6.6			
							130	520	90.2			
H475_Milled-Residue	OZW428U2	−25.8	106.9	1.1	12.46	0.15	20,440	19,860	95.4	20,140	19,805	Older
H653_Top	OZY112U1	−11.0	320.0	10	25.86	0.80	13,200	12,020	95.4	12,710		
H653_Middle	OZY113U1	−11.0	19.7	0.2	13.51	0.77	20,470	18,370	95.4	19,380		
H653_Base	OZY817U1	−11.0	41.8	0.4	2.50	0.34	35,580	31,290	95.4	33,540		
H204_Top-1	OZV046U1	−11.4	450.0	10	35.26	0.20	9180	9140	4.0	9350		
							9220	9200	1.5			
							9470	9240	94.5			

continued on next page

Sample code	Laboratory code	δ^{13}C per mil	C mass (μg)	Mass Err (μg)	Percent modern carbon (pMC)	±1σ error	Calibrated date (95.4% probability range)(years cal. yr B.P.)					
							from	to	%	Median	Discrepancy	Younger/ Older
H204_Top-1-Residue	OZV046U2	−21.1	94.015.0	1.0 0.15	36.46	0.29	8680	8650	1.5	8950	400	Younger
							8690	8680	0.1			
							9140	8690	97.3			
							9200	9180	0.7			
							9230	9230	0.3			
H204_Top 2	OZW430U1	−11.0	24.3	0.25	29.07	0.99	12,180	10,580	96.6	11,400		
							12,200	12,190	0.2			
							12,300	12,210	1.8			
							12,400	12,330	1.4			
H204_Top 2-Residue	OZW430U2	−25.0*	47.0	0.5	13.99	0.61	19,910	18,290	95.4	19,060	7660	Older
H076_Top	OZY818U1	−11.0	780.0	10	23.67	0.40	13,610	13,080	99.6	13,370		
							13,700	13,690	0.4			
H076_Middle 1	OZV045U1	−9.4	89.0	0.9	7.04	0.08	25,840	25,350	95.4	25,620		
H076 Middle 1-Residue	OZV045U2	−22.5	43.9	0.5	43.06	0.29	7680	7490	95.4	7590	18,030	Younger
H076_Middle 2	OZY819U1	−11.0	98.0	1.0	5.33	0.34	28,660	26,660	95.4	27,690		
H076_Base	OZY820U1	−11.0	91.0	0.9	0.75	0.28	48,820	37,300	95.4	43,120		
J040_Top	OZY890U1	−11.0	112.4	1.2	45.39	0.96	7510	6790	99.5	7190		
							7560	7540	0.5			
J040_Top-Residue	OZY890U2	−25.0*	210.0	10	13.45	0.1	19,593	19,196	95.4	19,401	12,211	Older
J040_Middle 1	OZY889U1	−12.1	290.0	10	20.95	0.41	15,240	14,120	95.4	14,710		
J040_Middle 1-Residue	OZY889U2	−25.0*	41.0	0.4	17.32	0.27	17,453	16,623	95.4	17,057	2347	Older
J040_Middle 2	OZY888U1	−10.5	82.7	0.8	17.33	0.29	17,470	16,600	95.4	17,050		
J040_Middle 2-Residue	OZY888U2	−25.0*	210.0	10	14.53	0.11	18,854	18,573	95.4	18,721	1671	Older
J040_Base	OZY887U1	−11.0	10.8	0.1	9.36	0.30	23,520	22,380	95.4	22,890		
J040_Base-Residue	OZY887U2	−25.0*	96.0	1.0	17.41	0.25	17,393	16,588	95.4	16,996	5894	Younger

continued on next page

Sample code	Laboratory code	δ^{13}C per mil	C mass (μg)	Mass Err (μg)	Percent modern carbon (pMC)	±1σ error	Calibrated date (95.4% probability range)(years cal. yr B.P.)					
							from	to	%	Median	Discrepancy	Younger/ Older
H739_Top	OZY895U1	−11.0	68.3	7.0	35.98	1.57	9939	8320	99.0	9090		
							10,007	9990	0.2			
							10,125	10,060	0.8			
H739_Top-Residue	OZY895U2	−25.0*	500.0	10	11.59	0.09	21,039	20,609	95.4	20,818	11,728	Older
H739_Bottom	OZY896U1	−11.0	41.0	0.42	22.29	0.45	14,370	13,460	95.4	13,890		
H739_Bottom-Residue	OZY896U2	−25.0*	85.0	9.0	13.85	0.26	19,508	18,789	95.4	19,117	5227	Older
H754	OZW427U1	−11.0	27.1	0.4	45.17	0.35	7430	7160	95.4	7280		
H754-Residue	OZW427U2	−25.0*	41.0	0.42	31.25	0.32	10,690	10,260	95	10,490	3210	Older
H301	OZV049U1	−12.7	39.0	0.4	82.89	0.61	1490	1280	98.2	1360		
							1510	1500	1.8			
H301-Residue	OZV049U2	−25	35.5	0.4	85.06	0.77	990	1020	4.7	1170	190	Younger
							1050	1300	95.3			
H299	OZV048U1	−10.8	1,090	10	78.82	0.30	1730	1880	95.4	1810		
H299-Residue	OZV048U2	−22.5	41.4	0.4	77.65	0.54	1760	1760	0.1	1950	140	Older
							2090	1820	99.9			
H295	OZV047U1	−13.0	113.4	1.2	55.39	0.38	5490	5320	72.3	5440		
							5580	5500	27.7			
H295-Residue	OZV047U2	−22.5	21.0	0.2	55.89	0.56	5190	5050	19.2	5360	80	Younger
							5490	5210	69.6			
							5580	5500	11.2			
H207	OZV034U1	−7.0	410.0	10	16.71	0.11	17,650	17,230	95.4	17,460		
H207-Residue	OZV034U2	−22.5	51.2	0.5	37.93	0.33	8650	8390	98.6	8520	8940	Younger
							8700	8670	1.4			
H347	OZV050U1	−13.6	160.0	10	7.24	0.12	25,710	25,060	95.4	25,400		
H347-Residue	OZV050U2	−22.5	89.2	0.9	60.91	0.42		4160	0.9	4380	21,020	Younger
								4180	2.1			
								4230	97.0			
H234	OZV035U1	−8.4	280	10	49.81	0.12	18,690	18,330	95.4	18,510		
H234-Residue	OZV035U2	−22.5	71.9	0.7	14.92	0.44	6254	6210	5.5	6360	12,150	Younger
							6494	6260	94.5			

*The value is assumed.

Comparing radiocarbon ages of residue and acid-soluble fractions in accretions

By producing both a consistent sequence of oxalate-fraction radiocarbon ages through the accretion microstratigraphy (e.g., Samples J030, H653, H076, and J040) and replicating ages along individual layers (e.g., Sample H076; Table 1), this study demonstrates closed system behavior with respect to carbon for multiple, individual accretions. However, residue fractions from the same stratigraphies do not consistently return sequenced ages with the residue fraction dated at younger than the corresponding acid-soluble fraction in some samples and older in others (Fig. 7). The residue in oxalate-rich accretions is reported to consist of inert solids, such as silica, pollen, charcoal, and nonreactive residual organic matter, suggested to originate from older materials, incorporated into accretion layers via dust and aerosols during growth intervals (*5*). However, in this study, while five radiocarbon determinations on nonoxalate residue fractions returned ages considerably older [>5 thousand years] than the corresponding acid-soluble fraction measurements, thus supporting this proposed mechanism, 11 generated radiocarbon ages considerably younger (Table 1).

We explain this result using the proposed mechanism of formation for oxalate accretions. During intervals inconducive to microbial activity, oxalate deposition ceases and windblown material may accumulate on these same surfaces. This material may include carbon-bearing detritus, such as charcoal and organic debris, with the aeolian pyrogenic carbon sourced from seasonally burnt spinifex grass carrying a maximum inbuilt age of up to ~1000 years (*31*). Where this material adheres or is trapped in depressions on the depositional surface, it is relatively stable and so may persist for an extended period, becoming incorporated into the developing mineral accretion. Whether these residues are dated at older or younger than the corresponding oxalate-fraction may depend on whether the carbon-bearing detritus included in the micromilled sample was deposited above or below the target layer, i.e., whether it accumulated on the accretion surface for an extended time before (e.g., sample H754; Table 1 and Fig. 7) or following (e.g., samples H234, H347, and H207; Table 1 and Fig. 7) oxalate deposition. The relatively coarse scale of the micromill sampling (50 to 100 μm) compared to the thinnest mineral layers may contribute to this explanation, making it difficult to avoid carbon-bearing detritus above or below the target oxalate (Fig. 7). Where the difference between the age of the oxalate-derived carbon and the residue carbon is small (<1 ka; e.g., samples J030-Middle 1, H204-Top 1, H301, H299, H295; Table 1), it is likely that the formation of the oxalate-rich layer and the deposition of detrital material are roughly contemporaneous.

However, where a residue fraction returns an age substantially younger than both the corresponding acid-soluble fraction and the acid-soluble fraction from the subsequent layer (Fig. 7), the carbon in the residue fraction cannot originate from material deposited on the accretion surface during a hiatus in oxalate deposition between stratigraphically sequenced layers. The absence of sequenced radiocarbon ages on residue fractions in accretions that do demonstrate stratigraphically consistent ages for the acid-soluble mineral fractions suggests that the residue material may simply not be suitable for radiocarbon dating, potentially demonstrating open-system behavior and unreliable ages. These results imply that, without separation of the two fractions, bulk mineral radiocarbon age determinations on the accretions will almost certainly be incorrect (Table 1), aggregating both inherited and depositional components.

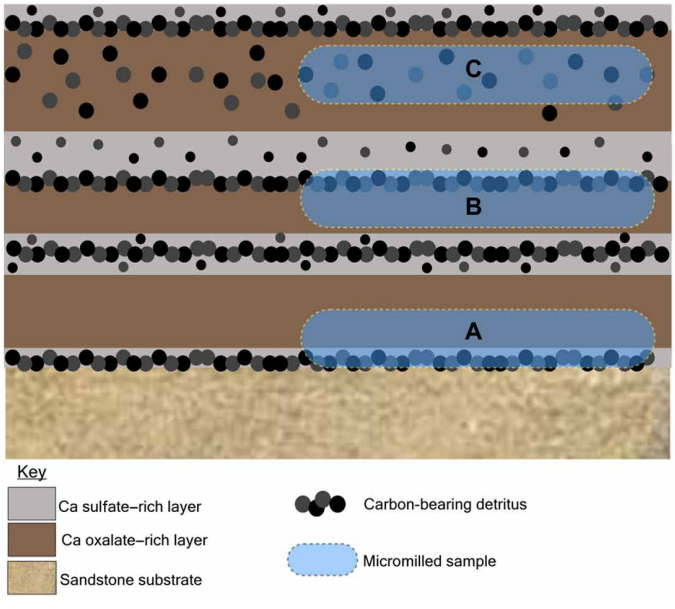

Fig. 7. Proposed relationships between oxalate and residue derived carbon in layered accretions. Residue fractions dated at older or younger than the corresponding acid-soluble fraction may depend on whether the carbon-bearing detritus included in the micromilled sample was deposited above or below the target layer. The rate of carbon-bearing detritus deposition varies over the accretion growth interval with areas of high detrital concentration indicated by the density of black and gray dots. (**A**) The residue fraction is older than the acid-soluble fraction. (**B**) The residue fraction is younger than the acid-soluble fraction. (**C**) The residue and acid-soluble fractions are approximately equal age.

Identifying regionally synchronous oxalate growth intervals in layered accretions

Distinctive layers identified in most accretions were assigned a number (Fig. 8A), enabling the identification of similar patterns in the internal stratigraphies of accretions collected in separate rock shelters across the area. In particular, two closer spaced, light-colored layers (layers 3 and 4, Fig. 8A) of approximately equal width, generally occurring toward the top of the cross section of many samples, represent a particular point of correlation between accretions collected in separate shelters. Although radiocarbon dates for 14 accretions are reported here, the distinct layer pattern identified in Fig. 8 has been identified in many further, as yet undated, oxalate accretions, so this sequence appears to be a general characteristic of these materials on at least a regional scale.

The radiocarbon dates can test the apparent layer correlation within the accretions across sites separated by distances of up to 90 km (Figs. 1 and 8). Samples milled from oxalate-rich layers in accretions collected at eight separate shelters bracket the deposition of marker layers 3 and 4 to between 11.4 and 13.4 ka cal B.P. (Fig. 8). Below this, an oxalate-rich layer, milled between marker layers 2 and 3 in eight accretions, indicates deposition between 13.4 and 19.4 ka cal B.P. (Figs. 8, B and D) and samples milled between marker layers 1 and 2, in four accretions, indicate that this material was deposited between 21.2 and 27.7 ka cal B.P. Samples milled below marker layer 1 in two separate accretions suggest that oxalate-rich material was deposited between 31.0 and 43.1 ka cal B.P. (Fig. 8). Radiocarbon samples milled from near surface layers in four further

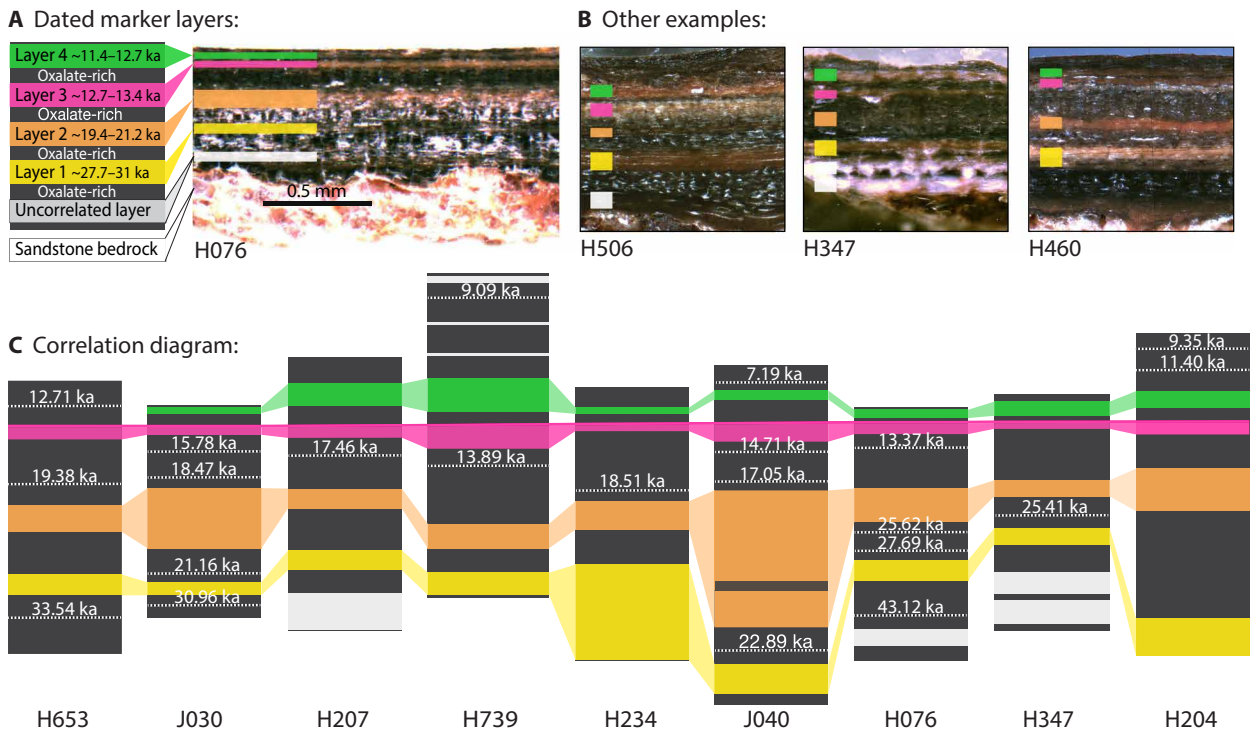

Fig. 8. Correlations between oxalate mineral accretion sequences. These correlated layers indicate synchronous growth patterns in nine accretions sampled in separate rock shelters across the northeast Kimberley separated by distances of up to 90 km. (**A**) shows a typical example of the visible light and dark layers in sample H076 identifying four distinctive light-colored (oxalate-poor) marker layers together with their range of inferred ages determined on the darker oxalate-rich layers between them. (**B**) Polished cross sections for three other accretions (H506, H347, and H460). (**C**) Schematic cross sections of nine accretion samples that have been aligned to the top of the pink layer (layer 3), which approximates to the start of the Holocene. Individual radiocarbon ages on micromilled acid-soluble fractions are shown by the horizontal dashed lines. Several other noncorrelated light layers that are younger or older than these marker layers are also indicated as pale gray bars in some samples. Photo credit: Helen Green, University of Melbourne.

accretions (H295, H299, H301, and D754) returned ages between 0.3 and 7.2 ka cal B.P., suggesting that an interval of growth occurred during the Holocene (Table 1). However, this growth was not represented in most of the samples (Fig. 8D), suggesting that their growth has been inactive for a considerable period.

The biological formation mechanism proposed for calcium oxalate deposition (*2*, *13*, *14*, *16*, *17*, *24*) demonstrates a link between environmental conditions and intervals of accretion growth. Alternating layering within stratigraphies indicates formation during discrete depositional events, influenced by shifting but repeating environmental conditions (*32*, *33*). The radiocarbon dates presented here (Table 1 and Fig. 8C) suggest that information relating to climate variability from before the last glacial maximum through the deglaciation to the Holocene could be decipherable from the laminated accretions, with some several millimeter-thick accretions encapsulating 30- to 40-ka time spans.

DISCUSSION

Accelerator MS (AMS) radiocarbon dating of up to four subsamples (per accretion) from oxalate-rich layers were dated in the microstratigraphic sequence of 14 accretion samples, often only 2 to 3 mm thick. We argue that the only feasible explanation for the consistent radiocarbon ages, both along individual layers and in strict stratigraphic sequence (Fig. 8), is that the radiocarbon dates are reliable and that closed system behavior has been maintained. The fine details of individual microlaminations (Fig. 4) preserved within these oxalate accretions also indicate that there has been no subsequent disturbance of the layering following initial deposition, especially by mechanisms such as dissolution and redeposition. A similar approach was used to assess the reliability of radiocarbon dating in oxalate-rich accretions at Carpenter's Gap shelter in the southern Kimberley (see Fig. 1) (*20*). Here, radiocarbon ages confirmed stratigraphically consistent layers both within a single accretion and between multiple, buried accretions and their overlying sediments.

The proven reliability of this application of radiocarbon dating and the relationship between many of the microlaminated oxalate-rich accretions and either engravings or paintings shows that these materials can be used for dating rock art across northern Australia as has been applied elsewhere (*5*, *9*, *21*, *25*), and while determining specific dates for individual motifs was not the primary objective of this study, some age limits can nevertheless be deduced. Sample H475 (Fig. 2D and Table 1), for example, is an interesting case in point, demonstrating the potential of such accretions for dating both geomorphic processes and rock art. The horizontal fracture in Fig. 2D must clearly be older than the age of 1.86 ka for oxalate material to develop within it, and the Gwion-style anthropomorphic figure divided by the fracture must be older than this in turn. This age is consistent with independently established ages for this art style (*34*). Furthermore, all of the cupules on the shelter surface sampled in

Fig. 2B appear to have been ground into the existing oxalate-rich accretion so that a maximum age of 1.37 ka (sample 301; Table 1) can be established for their production on this surface. In many cases, bracketing ages may be possible where the engravings occur within the laminated sequence. Many of the grooves engraved into some of the thicker, laminated accretions show evidence of overgrowth by younger oxalate material indicating that the engravings must be older than the youngest dated layers. However, perhaps the most notable feature of oxalate-rich accretions across the north Kimberley study area in tropical northern Australia is that the distinctive patterns observed in their internal laminations appear remarkably similar, not only within a single rock shelter (*20*, *25*) but also in many sites across the region separated by distances of up to 90 km (Fig. 8).

The identification of regionally consistent patterns of correlated microlaminations establishes an initial master chronology for oxalate-rich accretions in this region, ranging from ~0.3 to 43 ka (Fig. 8 and Table 1), a period during which paleoenvironmental and paleoclimatic conditions in the Kimberley are known to have fluctuated substantially (*32*). Finer-scale variability observed in the lamination patterns between samples is likely the result of local microclimates and shelter specific conditions also influencing accretion formation. However, the identification of broadly similar patterns in the internal stratigraphies of multiple, widely separated accretions strongly suggests that their formation must be largely controlled externally by variations in regional environmental conditions. Individual layers are interpreted to represent discrete depositional periods, probably related to repeating wet-dry cycles. Accretion formation over time frames comparable to painted rock art (*34*–*36*) means these records of fluctuating environmental conditions may provide insight into changes in the art styles observed throughout this interval. Furthermore, the major features of this sequence of light and dark layers can often be recognized on a broken accretion surface with a hand lens so that a first approximation of age might even be obtained simply by examination in the field (e.g., Fig. 3B).

Further work to identify the specific microbial communities responsible for calcium oxalate precipitation, and the conditions under which they flourish may clarify links to more specific paleoenvironmental conditions. The evident stability of the radiocarbon system in these materials over extensive time spans and distances strongly suggests that other systems, such as stable isotopes, might further expand the potential of these widespread deposits for interpreting paleoenvironmental conditions. Comparable layered oxalate mineral accretions are found across northern Australia [e.g., (*3*)] and probably in many other parts of the world, offering considerable potential for radiocarbon dating of associated rock art, for calibrating the rates of local geomorphic processes, and as a previously unexplored terrestrial paleoenvironmental archive directly relevant to the period of human habitation.

MATERIALS AND METHODS

Field sampling and sample preparation

Seventy-seven oxalate-rich accretions, collected from 41 rock shelters across the northeast Kimberley (Fig. 1), during both the wet and dry seasons of 2014 to 2019 have been characterized by the authors (*11*, *12*). Key accretion features (color, texture, and thickness), their occurrence within the shelters (with reference to sunlight, moisture, angle of the depositional surface), and, where relevant, their spatial association with rock art were recorded. Samples were selected based on their association with rock art, on whether they exhibited the key characteristics identified in (*11*) and (*12*), and the ability to remove intact fragments from accretion base to surface. Sampling is detailed in (*11*) and (*12*). Where sufficient material was sampled, accretions were split in the laboratory, with one half analyzed using a range of techniques (*11*, *12*) to characterize the mineralogy and structure and the other half mounted in epoxy resin and polished on a cross section for examination of the layered internal structure. Here, 18 samples are selected for further analyses based on their internal stratigraphies and high oxalate content, with 14 of these accretions subsampled for radiocarbon dating.

Micro-CT analyses

To confirm the apparent continuity of accretion layers in three-dimensional cross section and two dimensions (*11*, *12*), micro-CT imaging was used to investigate the internal structure of four samples (J030, J040, H739, and H076) using a Waygate Technologies Nanotom M scanner at the University of Melbourne. Undulations or irregularities in the spatial positioning of the laminations in three dimensions may result in the mixing of carbon-bearing components of different ages during micromilling of radiocarbon dating samples, while small fissures (Fig. 4) penetrating the layer sequence may allow for younger calcium oxalate minerals to precipitate in older layers. The application of this prescreening process to layered accretions showed that such instances were rare and that optical examination is sufficient to avoid potentially problematic areas in most samples. However, in complex samples, micro-CT imaging is a useful tool in enabling the identification of clear, continuous layers free of fissures or stratigraphic inconsistencies that may compromise closed-system conditions with respect to carbon and is consequently important for the production of reliable age estimates in some instances when paired with pretreatment procedures, allowing for compound isolation radiocarbon dating of these materials.

Samples were mounted on a small glass rod and placed as close to the x-ray source as possible to maximize magnification on the detector and to achieve the highest possible resolution. Sample sizes were typically 2 mm by 5 mm and scan resolutions ranged from 2 to 5.56 μm. X-ray source energy was optimized to each sample and background measurement improved sample contrast in the final x-ray images. Samples were scanned for 10 min, collecting >1000 two-dimensional x-ray images through a 360° sample rotation.

The volume reconstruction of the micro-CT data was performed using Phoenix datos|x reconstruction software (GE Sensing & Inspection Technologies) applying a median filter and region of interest filter during reconstruction. The data were exported as 16-bit volume files for analysis using the Avizo (Thermo Fisher Scientific) software suite. Each dataset was then exported as a series of .tiff files imaging cross-sectional slices through the micro-CT volume.

The data for each sample were orientated to create two primary views of the sample along the three axes. First, cutting a cross section roughly parallel with the layers in the sample (*yz* planes). Second, cutting a cross section perpendicular to the layers (*xy* planes). Animated visualizations may be found in the Supplementary Materials.

Porosity of the glazes was calculated to show the amount of empty space (interpreted as cracks, partings, or holes) within each of the four samples, appearing as black to dark gray areas in the reconstructions. A sample mask was created using the Avizo interactive thresholding tool and used to calculate the total volume of the

sample (including pore space). The porosity was calculated from the volume fraction of masked "pore space" relative to the total volume of the sample. This process is repeated for each cross-sectional image taken through the sample parallel to layering and the data used to summarize porosity within each sample in comparison to its layering (Fig. 4).

Compositional layering in oxalate-rich accretions

Polished mounts of samples identified as containing significant proportions of calcium oxalate were examined under the microscope, and those with clear, consistent internal layering were selected for further analyses. Electron probe microanalysis (EPMA) and LA-ICPMS analyses were used to produce two-dimensional maps of key elements (carbon, calcium, and sulfur) within individual layers of the microstratigraphy. The two techniques are complementary in that EPMA, while not having the same low detection limit of LA-ICPMS is capable of resolving smaller areas of interest because of the smaller beam diameter. EPMA is also generally considered nondestructive, while LA-ICPMS ablates tracks in the accretion material that are ~40 μm wide and ~60 μm deep. Elemental maps were used to guide micromilling of individual lamina for targeted radiocarbon dating with the presence of elevated carbon and/or the presence of elevated calcium and the absence of sulfur used to identify areas of calcium oxalate.

Laser ablation trace element mapping

Trace element maps were produced using LA-ICPMS analyses, performed on an Agilent 7700x quadrupole MS, coupled to a Lambda Physik COMPex ultraviolet 193-nm excimer laser system at the University of Melbourne using a S-155 ablation cell. Samples were ablated under helium with an argon carrier gas. Before laser ablation analysis, samples were mounted in a "freeform" sample holder and imaged at high resolution on a flatbed scanner. The resulting images, referenced to the coordinate system of the ablation cell, could then be used as a base layer upon which to overlay the laser ablation element concentration "maps." The maps were produced by analyzing the material liberated from a series of parallel ablation tracks across the sample surface, oriented perpendicular to the growth banding. The analysis protocol used a scan speed of 40 μm s^{-1}, with a spot size of 40 μm, a pulse rate of 10 Hz, and a laser fluence of ~2.5 J cm^{-2}. NIST SRM 612 was used as the primary calibration material. In all laser analyses, the elements for which data are reported are Al, Si, Ca, S, Mg, P, K, and Mn with an estimated precision of elemental concentrations of ca. <5%. All data were reduced using Iolite software (*37*), with data deconvolution as described in (*38*).

Electron microprobe element mapping

Accretions were selected for EPMA on the basis of the clear and consistent internal layering and oxalate content. Mounted samples were analyzed using a JEOL JXA-8530F field emission electron microprobe at the University of Melbourne after applying a carbon coating to a thickness of 250 Å. This coating increases the carbon background, but provided that the carbon content of the accretion (generally a few percent) is above this background level, the carbon distribution can be qualitatively mapped. Gold coating was not considered because of the absorption of carbon x-rays at any coating thickness, decreasing the carbon sensitivity. Four elements were measured by wavelength dispersive spectrometers (WDSs), and the balance was measured by energy dispersive spectrometer (EDS). This study focuses on elements, such as carbon (C), sulfur (S), phosphorus (P), and calcium (Ca), relevant to identifying target material for radiocarbon dating, with the C measured on LDE2 WDS, the S and P on EDS, and the Ca on PETL WDS.

Radiocarbon age measurements

Microsampling of mounted accretion fragments was performed with a specialized New Wave MicroMill held in the School of Geography at the University of Melbourne, designed for sampling small objects such as microlaminated speleothems. The MicroMill comprised a dental drill with a 0.25-mm bit fixed over a computer-controlled X-Y-Z sample stage, stereo microscope, and a high-resolution digital camera. All components of the micromilling system were controlled by software specifically designed for this purpose to sample tracks specified onscreen by the operator. Powdered samples were milled to a depth of 0.25 mm from target layers in 14 separate accretions. EMPA and trace element mapping from LA-ICPMS were initially used to guide sampling of suitable layers, avoiding any areas demonstrating obvious discontinuities or unusual material identified optically in cross section and using micro-CT imaging. Once the darker layers had been identified as consistently containing higher proportions of oxalate, optical examination was sufficient for other samples in identifying compact and continuous layers likely to be suitable for radiocarbon dating. Multiple samples were collected along the same individual layers in some cases (sample H076; Table 1) and across a sequence of layers through the glaze microstratigraphy in others (samples J030, H653, H076, and J040; Table 1). The powder generated by milling each individual track was collected by hand using a micro spatula under the microscope and placed in a Teflon beaker, sealed with parafilm, and sent to the Australian Nuclear Science and Technology Organisation for pretreatment and AMS radiocarbon measurement. To avoid cross contamination, sampling tools and the sample surface were swabbed with ethanol between sample extractions.

Chemical pretreatment of the milled powders followed the protocol described by Jones *et al.* (*5*) and validated by Dumoulin *et al.* (*23*), separating the oxalate mineral component before measurement. This avoided contamination by carbon-bearing residues. The standard process and equipment used to convert most pretreated samples into graphite targets for AMS measurement are described in (*39*) and (*40*). Several quality control samples, including procedural blanks and check standards, were prepared together with all batches of oxalate samples using the same pretreatment stages on the same equipment as unknowns to assess the contamination in the course of sample handling. The final results were corrected for the blank determinations. All 14 samples used the 1-MeV VEGA or 10-MeV ANTARES AMS. ANTARES was used for the ultrasmall samples (*41*, *42*), and VEGA was used for larger samples (>0.1 mg) (*43*). Calibration was done with CALIB 7.1.0 (*44*) using the Southern Hemisphere dataset (*45*). $\delta^{13}C$ measurements are determined using an elemental analyser–isotope ratio MS values and relate solely to the graphite derived from the fraction that was used for the radiocarbon measurement. It is sometimes the case that the $\delta^{13}C$ of this fraction is not the same as that of the bulk material.

SUPPLEMENTARY MATERIALS

Supplementary material for this article is available at http://advances.sciencemag.org/cgi/content/full/7/33/eabf3632/DC1

REFERENCES AND NOTES

1. L. C. Prinsloo, Rock hyraces: A cause of San rock art deterioration? *J. Raman Spectrosc.* **38**, 496–503 (2007).
2. M. D. Monte, C. Sabbioni, G. Zappia, The origin of calcium oxalates on historical buildings, monuments and natural outcrops. *Sci. Total Environ.* **67**, 17–39 (1987).
3. A. Watchman, I. Ward, R. Jones, S. O'Connor, Spatial and compositional variations within finely laminated mineral crusts at Carpenter's Gap, an archaeological site in tropical Australia. *Geoarchaeology* **16**, 803–824 (2001).
4. N. Cole, A. Watchman, AMS dating of rock art in the Laura Region, Cape York Peninsula, Australia - protocols and results of recent research. *Antiquity* **79**, 661–678 (2005).
5. T. Jones, V. A. Levchenko, P. L. King, U. Troitzsch, D. Wesley, A. A. Williams, A. Nayingull, Radiocarbon age constraints for a Pleistocene-Holocene transition rock art style: The northern running figures of the East Alligator River region, western Arnhem Land, Australia. *J. Archaeol. Sci. Rep.* **11**, 80–89 (2017).
6. M. A. Smith, A. Watchman, J. Ross, Direct dating indicates a mid-Holocene age for archaic rock engravings in arid Central Australia. *Geoarchaeology* **24**, 191–203 (2009).
7. A. Watchman, Preliminary determinations of the age and composition of mineral salts on rock art surfaces in the Kakadu National Park, in *Ambrose & Mummery* (Australian National University Printing Press, 1987), pp. 36–42.
8. J. Russ, M. D. Pohl, C. L. von Nagy, K. L. Steelman, H. Hurst, L. Ashby, P. Schmidt, E. F. Padilla Gutiérrez, M. W. Rowe, Strategies for ^{14}C dating the Oxtotitlán cave paintings, Guerrero, Mexico. *Adv. Archaeol. Pract.* **5**, 170–183 (2017).
9. K. L. Steelman, R. Rickman, M. W. Rowe, T. W. Boutton, J. Russ, N. Guidon, AMS radiocarbon ages of an oxalate accretion and rock paintings at Toca do Serrote da Bastiana, Brazil, in *Archaeological Chemistry VI: Materials, Methods and Meaning*, K. Jakes, Ed. (ACS Symposium Series), pp. 22–35 (2002).
10. A. Hernanz, J. M. Gavira-Vallejo, J. F. Ruiz-López, Calcium oxalates and prehistoric paintings. The usefulness of these biomaterials. *J. Optoelectron. Adv. Mater.* **9**, 512–521 (2007).
11. H. Green, A. Gleadow, D. Finch, Characterisation of mineral deposition systems associated with rock art in the Kimberley region of northwest Australia. *Data Brief* **14**, 813–835 (2017a).
12. H. Green, A. Gleadow, D. Finch, J. Hergt, S. Ouzman, Mineral deposition systems at rock art sites, Kimberley, Northern Australia — Field observations. *J. Archaeol. Sci. Rep.* **14**, 340–352 (2017b).
13. A. Gorbushina, Life on the rocks. *Environ. Microbiol.* **9**, 1613–1631 (2007).
14. A. Mazel, A. Watchman, Dating rock paintings in the uKhahlamba-Drakensberg and the Biggarsberg, KwaZulu-Natal, South Africa. *Southern African Humanities* **15**, 59–73 (2003).
15. M. Del Monte, C. Sabbioni, Weddellite on limestone in the Venice [Italy] environment. *Environ. Sci. Technol.* **17**, 518–522 (1983).
16. G. M. Gadd, J. Bahri-Esfahani, Q. Li, Y. J. Rhee, Z. Wei, M. Fomina, X. Liang, Oxalate production by fungi: Significance in geomycology, biodeterioration and bioremediation. *Fungal Biol. Rev.* **28**, 36–55 (2014).
17. J. Russ, R. L. Palma, D. H. Loyd, T. W. Boutton, M. A. Coy, Origin of the whewellite-rich rock crust in the Lower Pecos region of southwest Texas and its significance to paleoclimate reconstructions. *Quatern. Res.* **46**, 27–36 (1996).
18. J. Russ, D. H. Loyd, T. W. Boutton, A paleoclimate reconstruction for southwestern Texas using oxalate residue from lichen as a paleoclimate proxy. *Quat. Int.* **67**, 29–36 (2000).
19. A. Watchman, Perspectives and potentials for absolute dating prehistoric rock paintings. *Antiquity* **67**, 58–65 (1993a).
20. A. Watchman, S. O'Connor, R. Jones, Dating oxalate minerals 20–45 ka. *J. Archaeol. Sci.* **32**, 369–374 (2005).
21. J. F. Ruiz, A. Hernanz, R. A. Armitage, M. W. Rowe, R. Viñas, J. M. Gavira-Vallejo, A. Rubio, Calcium oxalate AMS ^{14}C dating and chronology of post-Palaeolithic rock paintings in the Iberian Peninsula. Two dates from Abrigo de los Oculados (Henarejos, Cuenca, Spain). *J. Archaeol. Sci.* **39**, 2655–2667 (2012).
22. R. G. Bednarik, The dating of rock art: A critique. *J. Archaeol. Sci.* **29**, 1213–1233 (2002).
23. J.-P. Dumoulin, M. Lebon, I. Caffy, G. Mauran, A. Nankela, D. Pleurdeau, E. Delqué-Količ, C. Moreau, M. Perron, M. Sieudat, B. Thellier, L. Beck, Calcium oxalate radiocarbon dating: Preliminary tests to date rock art of the decorated open-air caves, Erongo Mountains, Nambia. Radiocarbon, 1-12. *Radiocarbon* **62**, 1551–1562 (2020).
24. M. J. Beazley, R. D. Rickman, D. K. Ingram, T. W. Boutton, J. Russ, Natural abundances of carbon isotopes (^{14}C, ^{13}C) in lichens and calcium oxalate pruina: Implications for archaeological and paleoenvironmental studies. *Radiocarbon* **44**, 675–683 (2002).
25. A. Watchman, Evidence of a 25,000-year-old pictograph in Northern Australia. *Geoarchaeology* **8**, 465–473 (1993b).
26. P. Veth, K. Ditchfield, M. Bateman, S. Ouzman, M. Benoit, A. P. Motta, D. Lewis, S. Harper; Balanggarra Aboriginal Corporation, Minjiwarra: Archaeological evidence of human occupation of Australia's northern Kimberley by 50,000 BP. *Australian Archaeology* **85**, 115–125 (2019).
27. G. Cazes, D. Fink, A. T. Codilean, R.-H. Fülöp, T. Fujioka, K. M. Wilcken, ^{26}Al/^{10}Be ratios reveal the source of river sediments in the Kimberley, NW Australia. *Earth Surf. Process. Landf.* **45**, 424–439 (2020).
28. M. B. Bodí, D. A. Martin, V. N. Balfour, C. Santín, S. H. Doerr, P. Pereira, A. Cerdà, J. Mataix-Solera, Wildland fire ash: Production, composition and eco-hydro-geomorphic effects. *Earth Sci. Rev.* **130**, 103–127 (2014).
29. W. Huang, E. Ertekin, T. Wang, L. Cruz, M. Dailey, J. DiRuggiero, D. Kisailus, Mechanism of water extraction from gypsum rock by desert colonizing microorganisms. *Proc. Natl. Acad. Sci. U.S.A.* **117**, 10681–10687 (2020).
30. V. A. Levchenko, A. Alan Williams, Time history of a human kidney stone determined by bomb-pulse dating. *Radiocarbon* **58**, 437–441 (2016).
31. D. Finch, A. Gleadow, J. Hergt, V. A. Levchenko, D. Fink, New developments in the radiocarbon dating of mud wasp nests. *Quat. Geochronol.* **51**, 140–154 (2019).
32. A. N. Williams, S. Ulm, T. Sapienza, S. Lewis, C. S. M. Turney, Sea-level change and demography during the last glacial termination and early Holocene across the Australian continent. *Quat. Sci. Rev.* **182**, 144–154 (2018).
33. D. S. Whitley, C. M. Santoro, D. Valenzuela, Climate change, rock coatings, and the archaeological record. *Elements* **13**, 183–186 (2017).
34. D. Finch, A. Gleadow, J. Hergt, V. A. Levchenko, P. Heaney, P. Veth, S. Harper, S. Ouzman, C. Myers, H. Green, 12,000-year-old aboriginal rock art from the Kimberley region, Western Australia. *Sci. Adv.* **6**, eaay3922 (2020).
35. R. Roberts, G. Walsh, A. Murray, J. Olley, R. Jones, M. Morwood, C. Tuniz, E. Lawson, M. Macphail, D. Bowdery, I. Naumann, Luminescence dating of rock art and past environments using mud-wasp nests in northern Australia. *Nature* **387**, 696–699 (1997).
36. J. Ross, K. Westaway, M. Travers, M. J. Morwood, J. Hayward, Into the past: A step towards a robust Kimberley rock art chronology. *PLOS ONE* **11**, e0161726 (2016).
37. C. Paton, J. Hellstrom, B. Paul, J. Woodhead, J. Hergt, *Iolite: Freeware for the Visualisation and Processing of Mass Spectrometric Data*, Vol. online (2011).
38. B. Paul, C. Paton, A. Norris, J. Woodhead, J. Hellstrom, J. Hergt, A. Greig, CellSpace: A module for creating spatially registered laser ablation images within the Iolite freeware environment. *J. Anal. At. Spectrom* **27**, 700–706 (2012).
39. Q. Hua, G. E. Jacobsen, U. Zoppi, E. M. Lawson, A. A. Williams, A. M. Smith, M. J. McGann, Progress in radiocarbon target preparation at the ANTARES AMS Centre. *Radiocarbon* **43**, 275–282 (2001).
40. Q. Hua, U. Zoppi, A. A. Williams, A. M. Smith, Small-mass AMS radiocarbon analysis at ANTARES. *Nucl. Instrum. Methods Phys. Res. B* **223**, 284–292 (2004).
41. B. Yang, A. M. Smith, Q. Hua, A cold finger cooling system for the efficient graphitisation of microgram-sized carbon samples. *Nucl. Instrum. Methods Phys. Res. B* **294**, 262–265 (2013).
42. B. Yang, A. M. Smith, Conventionally heated microfurnace for the graphitization of microgram-sized carbon samples. *Radiocarbon* **59**, 859–873 (2016).
43. K. Wilcken, M. Hotchkis, V. Levchenko, D. Fink, T. Hauser, R. Kitchen, From carbon to actinides: A new universal 1MV accelerator mass spectrometer at ANSTO. *Nucl. Instrum. Methods Phys. Res. B* **361**, 133–138 (2015).
44. M. Stuiver, P. Reimer, Extended ^{14}C data base and revised CALIB 3.0 ^{14}C age calibration program. *Radiocarbon* **35**, 215–230 (1993).
45. A. G. Hogg, Q. Hua, P. G. Blackwell, M. Niu, C. E. Buck, T. P. Guilderson, T. J. Heaton, J. G. Palmer, P. J. Reimer, R. W. Reimer, C. S. M. Turney, S. R. H. Zimmerman, SHCAL13 Southern Hemisphere calibration, 0–50,000 years cal BP. *Radiocarbon* **55**, 1889–1903 (2013).

Acknowledgments: We acknowledge and thank the Balanggarra Aboriginal Corporation, Rangers and Traditional Owners for permission to work on their Country and for support during fieldwork. In particular, we thank A. Unghango and family, the Waina family, and A Chalarimeri. Fieldwork support was provided by C. Myers, P. Heaney, S. Ouzman, S. Harper, S. Bradley, P. Hartley, N. Sundblom, C. Townsend, R. Maher, B. Maher, T. Tan, P. Turnbull, S. Ball, M. Maier, and P. Kendrick. The sites visited were relocated and recorded over decades by Dunkeld Pastoral Co. Pty. Ltd. and the Kimberley Visions Survey teams, J. Schmiechen, and the late G. Walsh. We thank P. Heaney for illustrations and management of the Filemaker Database at the University of Melbourne, R. Drysdale for the use of micromilling facilities in the School of Geography, the Melbourne TrACEES (Trace Analysis for Chemical, Earth and Environmental Sciences) Platform for access to the nanotom m micro-CT scanner, J. Black for technical support, and G. Hutchinson for electron microprobe analysis and data reduction in the School of Earth Sciences. We also thank A. Greig for assisting in LA-ICPMS trace element mapping and data reduction. Radiocarbon measurements and laboratory support from the Australian Nuclear Science and Technology Organisation (ANSTO) was provided by A. Williams, F. Bertuch, and B. Yang. Financial support for the Centre for Accelerator Science at ANSTO was provided by the Australian National Collaborative Research Infrastructure Strategy. H.G. thanks AINSE Ltd. for providing financial assistance through a Post Graduate Research Award to enable work on the radiocarbon analyses. H.G., C.M., and A.G. are members of the Science Advisory Committee for Rock Art Australia. **Funding:** This research was funded by an

Australian Research Council Linkage Projects LP130100501 and LP170100155 with Rock Art Australia as a funding partner and supported in kind by the Dunkeld Pastoral Co. Pty. Ltd., Western Australia (WA) Department of Biodiversity, Attractions and Conservation (DBAC), and Balanggarra Aboriginal Corporation especially for fieldwork. H.G. is supported by a fellowship in Rock Art Dating awarded by The Ian Potter Foundation to Rock Art Australia. **Author contributions:** This research is part of the multidisciplinary Kimberley Rock Art Dating project conceived and led by A.G. H.G., D.F., and J.M. collected and pretreated the samples, designed and performed the experiments, and analyzed and interpreted the results. Fieldwork was carried out by H.G., C.M., J.M., D.F., A.G., P.H., and V.A.L. Radiocarbon measurements and initial data reduction were performed by V.A.L. Laser ablation trace element mapping and data reduction were performed by H.G. H.G. wrote the manuscript draft with key editing from A.G. and R.P., with further input from all authors. **Competing interests:** The authors declare that they have no competing interests. **Data and materials availability:** All data needed to evaluate the conclusions in the paper are present in the paper and/or the Supplementary Materials and two earlier publications (*11*, *12*). At the request of Balanggarra Aboriginal Traditional Owners of the land where the samples were collected, the data do not include exact locations of rock art sites. Each sample collected from an archeological site was removed in close collaboration and consultation with local Traditional Owners from the Balanggarra native title region and approved under a Section 16 permit issued by the WA Department of Aboriginal Affairs (DAA). Additional permissions from the WA DBAC were obtained as required. Additional data related to this paper may be requested from the authors.

Submitted 24 October 2020
Accepted 25 June 2021
Published 13 August 2021
10.1126/sciadv.abf3632

Citation: H. Green, A. Gleadow, V. A. Levchenko, D. Finch, C. Myers, J. McGovern, P. Heaney, R. Pickering, Dating correlated microlayers in oxalate accretions from rock art shelters: New archives of paleoenvironments and human activity. *Sci. Adv.* **7**, eabf3632 (2021).